LETTER

doi:10.1038/nature21434

Simultaneous tracking of spin angle and amplitude beyond classical limits

Giorgio Colangelo[1], Ferran Martin Ciurana[1], Lorena C. Bianchet[1], Robert J. Sewell[1] & Morgan W. Mitchell[1,2]

Measurement of spin precession is central to extreme sensing in physics[1,2], geophysics[3], chemistry[4], nanotechnology[5] and neuroscience[6], and underlies magnetic resonance spectroscopy[7]. Because there is no spin-angle operator, any measurement of spin precession is necessarily indirect, for example, it may be inferred from spin projectors at different times. Such projectors do not commute, and so quantum measurement back-action—the random change in a quantum state due to measurement—necessarily enters the spin measurement record, introducing errors and limiting sensitivity. Here we show that this disturbance in the spin projector can be reduced below $N^{1/2}$—the classical limit for N spins—by directing the quantum measurement back-action almost entirely into an unmeasured spin component. This generates a planar squeezed state[8] that, because spins obey non-Heisenberg uncertainty relations[9,10], enables simultaneous precise knowledge of spin angle and spin amplitude. We use high-dynamic-range optical quantum non-demolition measurements[11–13] applied to a precessing magnetic spin ensemble to demonstrate spin tracking with steady-state angular sensitivity 2.9 decibels below the standard quantum limit, simultaneously with amplitude sensitivity 7.0 decibels below the Poissonian variance[14]. The standard quantum limit and Poissonian variance indicate the best possible sensitivity with independent particles. Our method surpasses these limits in non-commuting observables, enabling orders-of-magnitude improvements in sensitivity for state-of-the-art sensing[15–18] and spectroscopy[19,20].

Spin-based magnetometers monitor precession of the collective spin $\boldsymbol{F}$ of a magnetically sensitive atomic ensemble[1,3,21], whereas atomic clocks[2] and other atomic sensors[22] use pseudo-spin systems with equivalent quantum descriptions, but all are described by the SU(2) Lie algebra. Many optical interferometers are also SU(2) systems[23]. These SU(2) systems obey different uncertainty relations than do position/momentum or harmonic oscillator systems, with marked consequences for their quantum sensitivity limits. The classical quantity to be measured manifests as precession rate $\mathrm{d}\psi/\mathrm{d}t$ about a known axis, which we take to be x. This signal is not directly observable, because there is no quantum mechanical operator for spin angle ψ. Rather, it must be estimated, for example, from $F_z = |F_\rho|\cos(\psi)$, where $|F_\rho|$ is the spin amplitude in the y–z plane, itself an observable to be measured. Although some theoretical models assume F_ρ to be precisely known *a priori*, this assumption cannot be applied to most systems of interest—relaxation necessarily adds noise that is not knowable *a priori*[24]. We therefore require a multi-component measurement: of amplitude and angle, or equivalently F_y and F_z, in both cases requiring tracking of non-commuting observables.

Similarly, magnetic resonance techniques[20] use simultaneous amplitude and angle tracking to correlate spin-relaxation rate, which indicates the physical environment[19], with precession frequency, which indicates the chemical shift or, in imaging, the spin location[7]. In these applications, joint angle–amplitude dynamics contain the important signal.

For simple harmonic oscillator systems, it is well known that quantum measurement back-action couples angle and amplitude, or equivalently the quadratures X and P, as required to preserve the Heisenberg uncertainty relation $\delta X \delta P \geq 1/2$ (we take $\hbar = 1$ throughout). This limits angle tracking to the standard quantum limit[25] (SQL), with uncertainty $\delta\psi \sim N^{-1/2}$, where N is the mean number of excitations (here and throughout, '$\sim$' indicates equality to within a factor of order unity). In contrast, uncertainty principles do not prevent spin systems from being tracked beyond the SQL. As the spin components F_y and F_z precess about the x axis, they are governed by the Robertson (not Heisenberg) uncertainty relation[9]

$$\delta F_y \delta F_z \geq \frac{1}{2}\left|\langle [F_y, F_z]\rangle\right| = \frac{1}{2}\left|\langle F_x\rangle\right| \qquad (1)$$

In normal sensor operation, $\langle F_x\rangle$ is set to zero to allow large polarization in the F_y–F_z plane. Because it is a constant of the motion, $\langle F_x\rangle$ remains zero for all time and equation (1) places no limit on how precisely F_y and F_z can be simultaneously known or tracked. Arithmetic uncertainty relations[10] then set the relevant limit, $\mathrm{var}(F_y) + \mathrm{var}(F_z) \sim N^{2/3}$, which is well below the SQL $\mathrm{var}(F_z) \sim N$. Because N is typically about 10^6 in cold atom systems and about 10^{12} in atomic vapours, this $N^{1/3}$ advantage extends the quantum limits by orders of magnitude. Spin states with two sub-classical spin uncertainties have been studied theoretically as planar squeezed states[8].

Our discussion thus far indicates only the absence of uncertainty-principle barriers to precision spin tracking. We now outline a proof, given in Methods, that continuous quantum non-demolition (QND) measurement achieves this goal. The state evolution is illustrated in Fig. 1a and summarized here: F_z is coupled to an optical 'meter' variable S_z via the QND interaction $H_{\mathrm{eff}} = gF_zS_z$, where g is a coupling constant. The interaction with N_{L} photons imprints a signal proportional to F_z on the meter, which when measured reduces $\mathrm{var}(F_z)$ by an amount $\Delta_{\mathrm{m}} \sim g^2 N_{\mathrm{L}} \mathrm{var}^2(F_z)$. This same interaction rotates $\boldsymbol{F}$ about F_z by a random angle gS_z, which increases $\mathrm{var}(F_y)$ by $\Delta_{\mathrm{d}} \sim g^2 N_{\mathrm{L}} \mathrm{var}(F_x)$, which is much smaller than Δ_{m}, given that $\mathrm{var}(F_z) \gg 1$. Combining these effects, there is a net reduction of $\mathrm{var}(F_z) + \mathrm{var}(F_y)$, the total variance in the plane of precession. Precessing and under continuous measurement, F_z and F_y alternate roles as the measured and disturbed variable, and each experiences a net uncertainty reduction. When N_{L} reaches $1/(g^2N)$, the measurement benefit $\Delta_{\mathrm{m}} \sim N$ is of the order of the initial variance, while the in-plane back-action $\Delta_{\mathrm{d}} \sim 1$ is still negligible. Probing with this N_{L} also induces a negligible loss of coherence, so that the sensitivity to both angular and radial perturbations improves beyond classical limits. It is important to note that the quantum measurement back-action is not eliminated in this method; rather it is directed almost entirely to the F_x variable, which is never measured and acts as a depository for quantum uncertainty. A similar approach has been proposed for harmonic oscillators using auxiliary negative-mass oscillators to create uncertainty depositories[26–28].

[1]ICFO—Institut de Ciencies Fotoniques, The Barcelona Institute of Science and Technology, 08860 Castelldefels, Barcelona, Spain. [2]ICREA—Institució Catalana de Recerca i Estudis Avançats, 08015 Barcelona, Spain.

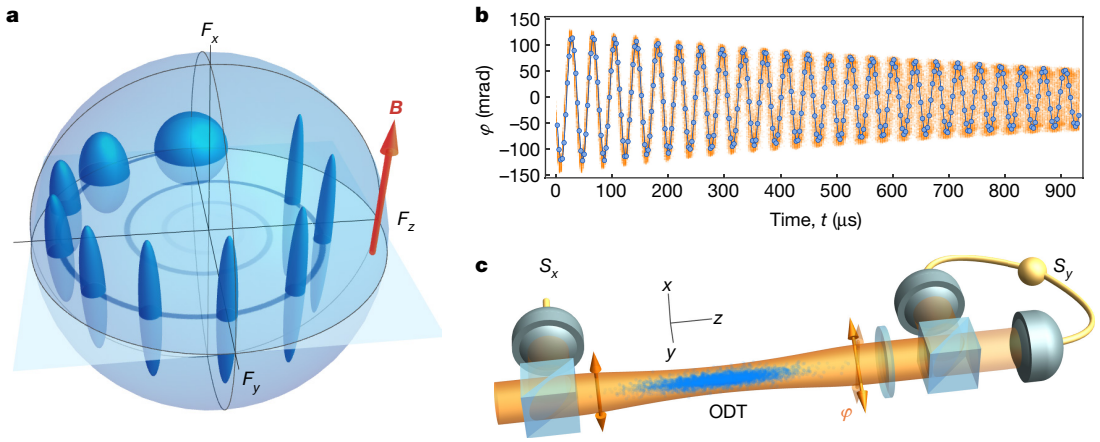

Figure 1 | Simultaneous, precise tracking of spin angle and amplitude. **a**, Bloch-sphere representation of the atomic state evolution. Ellipsoids show uncertainty volumes (not to scale) as the state evolves anticlockwise from an initial, F_y-polarized state with isotropic uncertainty. An x-oriented magnetic field $\boldsymbol{B}$ drives a coherent spin precession in the F_y–F_z plane. Quasi-continuous measurement of F_z produces a reduction in F_z and F_y variances, with a corresponding increase in var(F_x). **b**, Observed Faraday rotation angle $\varphi \propto F_z$ versus time t. Each circle shows the rotation angle from one vertically polarized pulse. A magnetic field of 37.6 mG produces the observed oscillation, while dephasing due to residual magnetic gradients and off-resonant scattering of probe photons cause the decay of coherence. Blue circles show a single, representative trace, overlaid on 453 repetitions of the experiment shown as orange dots. The time zero corresponds to the first probe pulse; the end of optical pumping is 58 μs earlier. **c**, Experimental geometry: 1.9×10^6 cold ^{87}Rb atoms are confined in a weakly focused single-beam optical dipole trap (ODT). Transverse optical pumping is used to produce F_y polarization. On-axis, 0.6-μs pulses with mean photon number 2.74×10^6 experience Faraday rotation by an angle $\varphi \propto F_z$. A polarimeter consisting of waveplates, a polarizing beamsplitter, high-quantum-efficiency photodiodes and charge-sensitive amplifiers measures the output Stokes component S_y. A reference detector before the atoms measures input Stokes component $S_0 = |S_x|$. The rotation angle is computed as $\varphi = \arcsin(S_y/S_x)$.

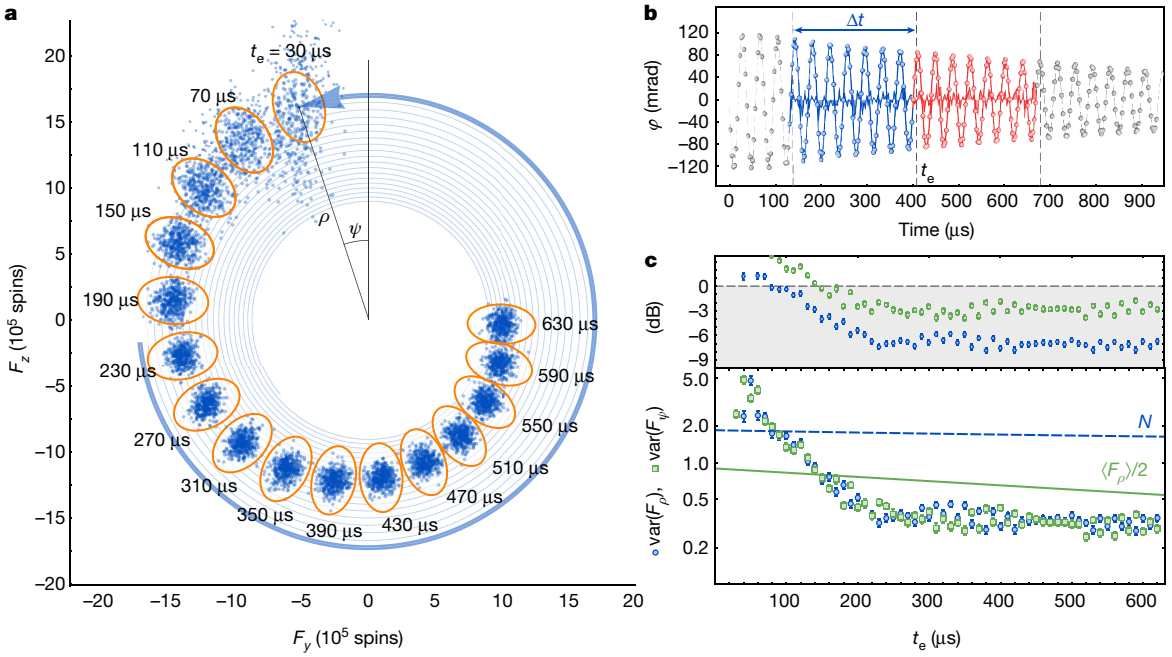

Figure 2 | Experimental results. **a**, Measured trajectories in the F_y–F_z phase space at different estimation times t_e. For each of the 453 traces shown in Fig. 1b, the function in equation (2) is fitted to the data to find predictive and confirming estimates $\boldsymbol{F}_1$ and $\boldsymbol{F}_2$, respectively, for (F_y, F_z) at time t_e. Fits for $\boldsymbol{F}_1$ and $\boldsymbol{F}_2$ use disjoint sets of data covering the ranges $t_e - \Delta t \le t_k < t_e$ and $t_e < t_k \le t_e + \Delta t$, respectively. A single fit is a tightly wound spiral, shown as a thin blue line; the thick arrow shows the trajectory from $t = 0$ to $t = t_e = 30$ μs. For clarity, we show results for t_e values spaced by 40 μs, slightly more than one Larmor period. Each point shows $\langle \boldsymbol{F}_1 \rangle + 100\boldsymbol{\mathcal{F}}$, where $\langle \boldsymbol{F}_1 \rangle$ is the mean over the 453 repetitions and $\boldsymbol{\mathcal{F}} \equiv \boldsymbol{F}_2 - \Gamma_{2,1}\Gamma_1^{-1}\boldsymbol{F}_1$ is the error of the best linear prediction (see Methods); the factor of 100 provides magnification for visualization purposes. Orange ellipses, with radial and azimuthal radii of 2σ, where $\sigma = 100\sqrt{\mathrm{CL}}$, show the relevant classical limits (CLs): Poisson (radial, CL = N) and SQL (azimuthal, CL = $\langle F_\rho \rangle/2$). **b**, Fits to estimate (F_y, F_z) for $t_e = 400$ μs and a measurement time $\Delta t = 270$ μs. Blue (red) shows fits based on prior (posterior) data. Shaded regions show fit residuals multiplied by 10. **c**, Evolution of tracking precision in decibels below the classical limits (top) and in spin units (bottom), for different t_e. Blue circles and green squares show radial and azimuthal components of $\Gamma_{\boldsymbol{F}_2|\boldsymbol{F}_1}$. Error bars show the ±1 standard error in the variance for 453 repetitions. Dashed blue and solid green curves show Poisson and SQL variances. These decrease during probing owing to loss of coherence and loss of atoms. No readout noise has been subtracted.

Realizing this in-principle advantage requires control of measurement dynamics[29] and incoherent effects[30], as well as low-noise non-destructive detection with high dynamic range[31]. We use an ensemble of $N = 1.9 \times 10^6$ cold ^{87}Rb atoms held in an optical dipole trap. The atoms are initially prepared in the F_y-polarized state by optical pumping and, owing to an applied magnetic field in the x direction, precess coherently in the F_y–F_z plane with Larmor period $T_L \approx 38\,\mu s$. The meter variable is the polarization of approximately 1-μs, off-resonance optical pulses, which experience Faraday rotation by an angle $\varphi = gF_z$ on the Poincaré sphere as they propagate through the atomic cloud. We probe the atoms with vertically polarized optical pulses, interspersed with horizontally polarized compensation pulses to dynamically decouple the spin alignment[12,13], that is, to produce the effective Hamiltonian $H_{\mathrm{eff}} = gF_zS_z$ without tensor light shifts. Previous experiments have demonstrated sub-projection-noise measurements of either angular[13] or amplitude[14] variables. To measure both, we use high-dynamic-range, shot-noise-limited optoelectronics[31] and nonlinear signal reconstruction to achieve sub-projection-noise readout sensitivity for rotation signals up to $\varphi \approx 100$ mrad (see Methods).

A representative sequence of measured Faraday rotation angles $\varphi(t_k)$, where t_k is the time of the kth pulse, for QND measurements spread over 1 ms is shown in Fig. 1b, and is well described by a free induction decay model that we use to estimate F_z and F_y at a time t_e:

$$\varphi(t) = g[F_z(t_e)\cos(\omega_L t_r) - F_y(t_e)\sin(\omega_L t_r)]e^{-t_r/T_2} + \varphi_0 \qquad (2)$$

where $t_r \equiv t - t_e$. The coupling constant g is found by an independent calibration, and the Larmor frequency ω_L, the coherence time T_2 and the offset φ_0 are found by fitting to the measured $\varphi(t_k)$ over the range $t_e - \Delta t \le t_k \le t_e + \Delta t$, where $\Delta t = 270\,\mu s$ (see Methods).

With these parameters fixed, we then use equation (2) to obtain a predictive estimate $\boldsymbol{F}_1 = \left(F_y^{(1)}, F_z^{(1)}\right)$ at time t_e using the measurements $\{\varphi(t_k)\}_{t_e - \Delta t \le t_k < t_e}$ from an interval Δt immediately before t_e, and to obtain a confirming estimate $\boldsymbol{F}_2 = \left(F_y^{(2)}, F_z^{(2)}\right)$ using the measurements $\{\varphi(t_k)\}_{t_e < t_k \le t_e + \Delta t}$ from the interval Δt after t_e. Because the classical parameters g, ω_L, T_2 and φ_0 are fixed beforehand, these are two linear, least-squares estimates of the vector $\boldsymbol{F}$ obtained from disjoint datasets. Estimating $\boldsymbol{F}$ for several values of t_e gives a predictive trajectory and a confirming one. We gather statistics over 453 repetitions of the experiment. Empirically, we find $\Delta t = 270\,\mu s$ minimizes the total conditional variance $\mathrm{tr}(\Gamma_{\boldsymbol{F}_2|\boldsymbol{F}_1})$ (see Methods), reflecting a trade-off of photon shot noise versus scattering-induced decoherence and magnetic-field technical noise.

Figure 2a shows the resulting mean predictive trajectory $\langle \boldsymbol{F}_1 \rangle$, which spirals slowly towards the origin owing to residual magnetic field gradient, and the discrepancy between the trajectories, $\boldsymbol{F}_2 - \boldsymbol{F}_1$. The scatter of this discrepancy rapidly decreases with increasing t_e, as more probe pulses become available for estimating $\boldsymbol{F}_1$, and reaches a steady state after about 250 μs of probing, at which point the number of pulses used for estimation is limited by Δt. With the optimum $\Delta t = 270\,\mu s$, the number of pulses is $N_p = 90$, the number of photons per pulse is n_L, and the total number of photons used to estimate $\boldsymbol{F}$ is $N_L = N_p n_L = 2.47 \times 10^8$.

To quantify the measurement uncertainty, we compute the vector conditional covariance $\Gamma_{\boldsymbol{F}_2|\boldsymbol{F}_1} = \Gamma_{\boldsymbol{F}_2} - \Gamma_{\boldsymbol{F}_2\boldsymbol{F}_1}\Gamma_{\boldsymbol{F}_1}^{-1}\Gamma_{\boldsymbol{F}_1\boldsymbol{F}_2}$ where $\Gamma_{\boldsymbol{v}}$ indicates the covariance matrix for vector $\boldsymbol{v}$, and $\Gamma_{\boldsymbol{uv}}$ indicates the cross-covariance matrix for vectors $\boldsymbol{u}$ and $\boldsymbol{v}$. Defining the polar coordinate system $(F_y, F_z) = \rho(-\sin\psi, \cos\psi)$, we identify the radial and azimuthal variances $\mathrm{var}(F_\rho) \equiv \hat{\rho}^{\mathrm{T}}\Gamma_{\boldsymbol{F}_2|\boldsymbol{F}_1}\hat{\rho}$ and $\mathrm{var}(F_\psi) \equiv \hat{\psi}^{\mathrm{T}}\Gamma_{\boldsymbol{F}_2|\boldsymbol{F}_1}\hat{\psi}$, respectively, where $\hat{\rho} \equiv (-\sin\psi,\ \cos\psi)^{\mathrm{T}}$ and $\hat{\psi} \equiv (-\cos\psi, -\sin\psi)^{\mathrm{T}}$ are radial and azimuthal unit vectors.

As shown in Fig. 2c, $\mathrm{var}(F_\psi)$ drops below the SQL of $\langle F_\rho \rangle/2$ after approximately 150 μs of probing, and remains below it to the limit of the experiment. No readout noise has been subtracted. Considering the steady-state region $t_e \ge 270\,\mu s$, $\mathrm{var}(F_\psi)$ is on average 2.9 dB below the SQL, and $\mathrm{var}(F_\rho)$ is on average 7.0 dB below the Poissonian variance N, to give a precision surpassing classical limits in both dynamical variables. For any given value of t_e, $\mathrm{var}(F_\rho)$ and $\mathrm{var}(F_\psi)$ have standard errors of approximately 0.3 dB, implying high statistical significance even without combining results for different t_e.

We have shown how quantum measurement back-action can be almost completely evaded in spin-based sensors and spectroscopies, enabling simultaneous tracking of spin angle and amplitude beyond classical limits, using the physics of planar squeezed states[8]. Our method is very close to practical application in the highest-performance atomic sensors: tracking of atomic spin precession by non-destructive optical measurement is already used in the highest-sensitivity magnetic field measurements[1] and is also being developed for optical lattice clocks[15]. The method is compatible with multi-pass[17] and cavity build-up methods[18], which greatly reduce incoherent scattering, the limiting factor in our experiment. Together, these advances promise orders-of-magnitude sensitivity improvement in extreme sensing, in applications ranging from studies of macromolecular dynamics[4] and geophysics[3], to non-invasive measurements of single-neurons[6] and brain dynamics[16].

Online Content Methods, along with any additional Extended Data display items and Source Data, are available in the online version of the paper; references unique to these sections appear only in the online paper.

Received 8 July 2016; accepted 19 January 2017.

1. Kominis, I. K., Kornack, T. W., Allred, J. C. & Romalis, M. V. A subfemtotesla multichannel atomic magnetometer. *Nature* **422,** 596–599 (2003).
2. Ludlow, A. D., Boyd, M. M., Ye, J., Peik, E. & Schmidt, P. O. Optical atomic clocks. *Rev. Mod. Phys.* **87,** 637–701 (2015).
3. Dang, H. B., Maloof, A. C. & Romalis, M. V. Ultrahigh sensitivity magnetic field and magnetization measurements with an atomic magnetometer. *Appl. Phys. Lett.* **97,** 151110 (2010).
4. Gomes, M. D. *et al.* ^{129}Xe NMR relaxation-based macromolecular sensing. *J. Am. Chem. Soc.* **138,** 9747–9750 (2016).
5. Wolf, T. *et al.* Subpicotesla diamond magnetometry. *Phys. Rev. X* **5,** 041001 (2015).
6. Jensen, K. *et al.* Non-invasive detection of animal nerve impulses with an atomic magnetometer operating near quantum limited sensitivity. *Sci. Rep.* **6,** 29638 (2016).
7. Plewes, D. B. & Kucharczyk, W. Physics of MRI: a primer. *J. Magn. Reson. Imaging* **35,** 1038–1054 (2012).
8. He, Q. Y., Peng, S.-G., Drummond, P. D. & Reid, M. D. Planar quantum squeezing and atom interferometry. *Phys. Rev. A* **84,** 022107 (2011).
9. Robertson, H. P. The uncertainty principle. *Phys. Rev.* **34,** 163–164 (1929).
10. Dammeier, L., Schwonnek, R. & Werner, R. F. Uncertainty relations for angular momentum. *New J. Phys.* **17,** 093046 (2015).
11. Grangier, P., Levenson, J. A. & Poizat, J.-P. Quantum non-demolition measurements in optics. *Nature* **396,** 537–542 (1998).
12. Koschorreck, M., Napolitano, M., Dubost, B. & Mitchell, M. W. Quantum nondemolition measurement of large-spin ensembles by dynamical decoupling. *Phys. Rev. Lett.* **105,** 093602 (2010).
13. Sewell, R. J., Napolitano, M., Behbood, N., Colangelo, G. & Mitchell, M. W. Certified quantum non-demolition measurement of a macroscopic material system. *Nat. Photon.* **7,** 517–520 (2013).
14. Béguin, J.-B. *et al.* Generation and detection of a sub-Poissonian atom number distribution in a one-dimensional optical lattice. *Phys. Rev. Lett.* **113,** 263603 (2014).
15. Lodewyck, J., Westergaard, P. G. & Lemonde, P. Nondestructive measurement of the transition probability in a Sr optical lattice clock. *Phys. Rev. A* **79,** 061401 (2009).
16. Sander, T. H. *et al.* Magnetoencephalography with a chip-scale atomic magnetometer. *Biomed. Opt. Express* **3,** 981–990 (2012).
17. Sheng, D., Li, S., Dural, N. & Romalis, M. V. Subfemtotesla scalar atomic magnetometry using multipass cells. *Phys. Rev. Lett.* **110,** 160802 (2013).
18. Hosten, O., Engelsen, N. J., Krishnakumar, R. & Kasevich, M. A. Measurement noise 100 times lower than the quantum-projection limit using entangled atoms. *Nature* **529,** 505–508 (2016).
19. Hall, L. T., Cole, J. H., Hill, C. D. & Hollenberg, L. C. L. Sensing of fluctuating nanoscale magnetic fields using nitrogen-vacancy centers in diamond. *Phys. Rev. Lett.* **103,** 220802 (2009).
20. Bienfait, A. *et al.* Reaching the quantum limit of sensitivity in electron spin resonance. *Nat. Nanotechnol.* **11,** 253–257 (2016).
21. Budker, D. & Romalis, M. Optical magnetometry. *Nat. Phys.* **3,** 227–234 (2007).

22. Miffre, A., Jacquey, M., Buchner, M., Trenec, G. & Vigue, J. Atom interferometry. *Phys. Scr.* **74,** C15–C23 (2006).
23. Yurke, B., McCall, S. L. & Klauder, J. R. SU(2) and SU(1,1) interferometers. *Phys. Rev. A* **33,** 4033–4054 (1986).
24. Colangelo, G. *et al.* Quantum atom–light interfaces in the Gaussian description for spin-1 systems. *New J. Phys.* **15,** 103007 (2013).
25. Braginsky, V. B., Vorontsov, Y. I. & Thorne, K. S. Quantum nondemolition measurements. *Science* **209,** 547–557 (1980).
26. Tsang, M. & Caves, C. M. Evading quantum mechanics: engineering a classical subsystem within a quantum environment. *Phys. Rev. X* **2,** 031016 (2012).
27. Polzik, E. S. & Hammerer, K. Trajectories without quantum uncertainties. *Ann. Phys.* **527,** A15–A20 (2015).
28. Møller, C. B. *et al.* Back action evading quantum measurement of motion in a negative mass reference frame. Preprint at https://arxiv.org/abs/1608.03613 (2016).
29. Smith, G. A., Chaudhury, S., Silberfarb, A., Deutsch, I. H. & Jessen, P. S. Continuous weak measurement and nonlinear dynamics in a cold spin ensemble. *Phys. Rev. Lett.* **93,** 163602 (2004).
30. Koschorreck, M., Napolitano, M., Dubost, B. & Mitchell, M. W. Sub-projection-noise sensitivity in broadband atomic magnetometry. *Phys. Rev. Lett.* **104,** 093602 (2010).
31. Ciurana, F. M., Colangelo, G., Sewell, R. J. & Mitchell, M. W. Real-time shot-noise-limited differential photodetection for atomic quantum control. *Opt. Lett.* **41,** 2946–2949 (2016).

Acknowledgements We thank G. Vitagliano, M. D. Reid, P. D. Drummond, G. Tóth, N. Behbood, M. Napolitano, S. Palacios, X. Menino and the ICFO mechanical workshop, and J.-C. Cifuentes and the ICFO electronic workshop. We also thank D. T. Campbell and M. M. Fría. Work supported by MINECO/FEDER, MINECO projects MAQRO (reference FIS2015-68039-P), XPLICA (FIS2014-62181-EXP) and Severo Ochoa grant SEV-2015-0522, Catalan 2014-SGR-1295, by the European Union Project QUIC (grant agreement 641122), European Research Council project AQUMET (grant agreement 280169) and ERIDIAN (grant agreement 713682), and by Fundació Privada CELLEX. L.C.B. was supported by the International Fellowship Programme 'La Caixa' - Severo Ochoa, awarded by the 'La Caixa' Foundation.

Author Contributions M.W.M. and G.C. conceived the project, experimental protocols were designed by G.C., F.M., R.J.S. and M.W.M., and the experiment was performed by G.C. and F.M. with help from L.C.B.; G.C. analysed the results with the help of R.J.S.; M.W.M. developed the theoretical model; and G.C., F.M., R.J.S. and M.W.M. wrote the manuscript with feedback from L.C.B.

Author Information Reprints and permissions information is available at www.nature.com/reprints. The authors declare no competing financial interests. Readers are welcome to comment on the online version of the paper. Correspondence and requests for materials should be addressed to G.C. (giorgio.colangelo@icfo.eu) or M.W.M. (morgan.mitchell@icfo.eu).

Reviewer Information *Nature* thanks F. Wilhelm-Mauch and the other anonymous reviewer(s) for their contribution to the peer review of this work.

METHODS

Faraday rotation probing of atomic spins. The effective atom–light interaction is given by the Hamiltonian

$$H_{\mathrm{eff}} = gS_zF_z \tag{3}$$

which describes a quantum non-demolition measurement of the collective atomic spin F_z, where the operators $F_\alpha \equiv \sum_i f_\alpha^{(i)}$ (with $\alpha = x, y, z$) describe the collective atomic spin, with $f_\alpha^{(i)}$ the spin orientation of individual atom spins. The optical polarization of the probe pulses is described by the Stokes operators $S_k = \frac{1}{2}(a_{\mathrm{L}}^\dagger, a_{\mathrm{R}}^\dagger)\sigma_k(a_{\mathrm{L}}, a_{\mathrm{R}})^{\mathrm{T}}$, in terms of Pauli matrices σ_k and creation operators $a_{\mathrm{L,R}}^\dagger$ and annihilation operators $a_{\mathrm{L,R}}$ for the left (L) and right (R) circular polarizations. The coupling constant g depends on the detuning from the resonance, the atomic structure and the geometry of the atomic ensemble and the probe beam, and is independently measured[30,32–35].

An input S_x-polarized optical pulse interacting with the atoms experiences a rotation by an angle $\varphi = gF_z$ because of the interaction given by equation (3). The transformation produced by the measurement on S_y is

$$S_y' = S_y\cos\varphi + S_x\sin\varphi$$

In our experiment, we measure S_x at the input by picking off a fraction of the optical pulse and sending it to a reference detector, and S_y' using a fast custom-built balanced polarimeter[31]. Both signals are recorded on a digital oscilloscope.

From the record of S_x and S_y', we calculate $\hat{\varphi}$, the estimator for φ:

$$\begin{aligned}\hat{\varphi} &= \arcsin\left(\frac{S_y'}{S_x}\right)\\ &= \arcsin\left(\sin\varphi + \frac{S_y}{S_x}\sqrt{1-\sin^2\varphi}\right)\\ &= \varphi + \frac{S_y}{S_x} + \frac{1}{2}\left(\frac{S_y}{S_x}\right)^2\tan\varphi + \mathcal{O}\left(\frac{S_y}{S_x}\right)^3\end{aligned}$$

Owing to shot noise, S_y/S_x is normally distributed with zero mean and variance $1/(2S_x) \approx 5\times10^{-7}$. The term containing $\tan\varphi$ thus describes a distortion of the signal at the approximately 10^{-6} level, which is negligible in the experiment.

Quantum limits for spin variances. Different classical limits provide benchmarks for the radial and azimuthal components of a spin precessing in the F_y–F_z plane. In general, these benchmarks describe the minimal noise of quantum states that describe uncorrelated particles. For our system of N spin-1 atoms, the lowest-noise uncorrelated state is the coherent spin state, which is defined as a pure product state in which each atom is fully polarized in the same direction. If this direction is $\hat{y}\cos\psi - \hat{z}\sin\psi$, then the azimuthal component $F_\psi = -F_y\sin\psi + F_z\cos\psi$ has variance

$$\mathrm{var}(F_\psi)_{\mathrm{SQL}} = \frac{\langle F_\rho\rangle}{2}$$

Any state that surpasses this limit implies entanglement among the atoms, and/or entanglement of the internal components of the individual atoms[36,37].

For the radial component $F_\rho = F_y\cos\psi + F_z\sin\psi$, the classical limit comes from the fact that accumulation of independent atoms into the ensemble is limited by Poisson statistics, $\mathrm{var}(N) = \langle N\rangle$, so that for $F = 1$

$$\mathrm{var}(F_\rho)_{\mathrm{Poisson}} = \langle N\rangle$$

Noise below this level can be produced by a strong interaction among the atoms during accumulation[14,38–40], or (as is the case here) by precise non-destructive measurement[18,35,41–45].

Operator-level description of back-action-evading measurement of two non-commuting spin observables. We consider a spin variable $\boldsymbol{F}$, defined by commutation relations $[F_x, F_y] = iF_z$ and cyclic permutations, precessing about the F_x axis and subjected to brief, non-destructive measurements of the F_z variable. We assume the precession during the measurement is negligible. In the measurement, the spin is coupled to the polarization of a probe pulse, described by the Stokes operators $\boldsymbol{S}$ with $[S_x, S_y] = iS_z$ and cyclic permutations. The initial state of the probe is a coherent state polarized along S_x, so that $|\langle S_x\rangle| = N_L/2$, $\langle S_y\rangle = \langle S_z\rangle = 0$ and $\mathrm{var}(S_y) = \mathrm{var}(S_z) = |\langle S_x\rangle|/2$. The system and meter are coupled by the quantum non-demolition Hamiltonian

$$H_{\mathrm{eff}} = gS_zF_z$$

which acts for unit time. The transformation produced is

$$\begin{aligned}S_x' &= S_x\cos(gF_z) - S_y\sin(gF_z)\\ S_y' &= S_y\cos(gF_z) + S_x\sin(gF_z)\\ S_z' &= S_z\\ F_x' &= F_x\cos(gS_z) - F_y\sin(gS_z)\\ F_y' &= F_y\cos(gS_z) + F_x\sin(gS_z)\\ F_z' &= F_z\end{aligned} \tag{4}$$

where primes indicate the output variables.

We assume a spin state in the F_y–F_z plane, that is, with $\langle F_x\rangle = 0$, and with zero initial cross-correlation, that is, $\mathrm{cov}(F_x, F_y) = \mathrm{cov}(F_x, F_z) = 0$. Owing to the zero mean of S_z, which is also independent of $\boldsymbol{F}$, the transformation preserves these statistics in the primed variables, for example

$$\begin{aligned}\mathrm{cov}(F_x', F_y') &= \mathrm{cov}(F_x, F_y)\langle\cos^2(gS_z) - \sin^2(gS_z)\rangle\\ &\quad + [\mathrm{var}(F_x) + \mathrm{var}(F_y)]\langle\cos(gS_z)\sin(gS_z)\rangle\\ &= 0\end{aligned}$$

We can compute the statistics of the output variables using

$$\langle\cos(gS_z)\rangle = \left\langle 1 - \frac{1}{2}g^2\mathrm{var}(S_z) + \mathcal{O}(g)^4\right\rangle = 1 - \frac{1}{4}g^2|\langle S_x\rangle| + \mathcal{O}(g)^4$$

and similar expansions for $\langle\cos^2(gS_z)\rangle$ and $\langle\sin^2(gS_z)\rangle$. The mean of F_y changes owing to the back-action as

$$\begin{aligned}\langle F_y'\rangle &= \langle F_y\rangle\langle\cos(gS_z)\rangle + \langle F_x\rangle\langle\sin(gS_z)\rangle\\ &= \langle F_y\rangle\langle\cos(gS_z)\rangle\\ &= \langle F_y\rangle - \frac{1}{4}g^2|\langle S_x\rangle|\langle F_y\rangle + \mathcal{O}(g)^4\end{aligned}$$

while the means of F_x and F_z are unchanged.

The variance of F_x is coupled to the variance of F_y, owing to the rotation about F_z by a random angle gS_z:

$$\begin{aligned}\mathrm{var}(F_x') &= \langle[F_x\cos(gS_z) - F_y\sin(gS_z)]^2\rangle - \langle F_y\rangle^2\langle\sin(gS_z)\rangle^2\\ &= \mathrm{var}(F_x)\langle\cos^2(gS_z)\rangle + \langle F_y^2\rangle\langle\sin^2(gS_z)\rangle\\ &= \mathrm{var}(F_x) + g^2|\langle S_x\rangle|\left[-\frac{1}{4}\mathrm{var}(F_x) + \frac{1}{2}\langle F_y^2\rangle\right] + \mathcal{O}(g^4)\end{aligned} \tag{5}$$

and similarly

$$\begin{aligned}\mathrm{var}(F_y') &= \langle[F_y\cos(gS_z) + F_x\sin(gS_z)]^2\rangle - \langle F_y\rangle^2\langle\cos(gS_z)\rangle^2\\ &= \langle F_y^2\cos^2(gS_z)\rangle + \langle F_x^2\sin^2(gS_z)\rangle - \langle F_y\rangle^2\langle\cos(gS_z)\rangle^2\\ &= \langle F_y^2\rangle\langle\cos^2(gS_z)\rangle - \langle F_y\rangle^2\langle\cos(gS_z)\rangle^2 + \langle F_x^2\rangle\langle\sin^2(gS_z)\rangle\\ &= \mathrm{var}(F_y) + g^2|\langle S_x\rangle|\left[-\frac{1}{4}\mathrm{var}(F_y) + \frac{1}{2}\mathrm{var}(F_x)\right] + \mathcal{O}(g^4)\end{aligned} \tag{6}$$

after noting that, to order g^3, $\langle\cos^2(gS_x)\rangle = \langle\cos(gS_x)\rangle^2$.

After the coupling, a projective measurement of S_y' provides information about F_z, with readout variance

$$\mathrm{var}_{\mathrm{RO}}(F_z) \approx \frac{1}{2g^2|\langle S_x\rangle|}$$

The approximation comes from a linearization of the expression for S_y' in equation (4), which, as discussed in Methods section 'Faraday rotation probing of atomic spins', introduces an error at the 10^{-6} level, negligible in this scenario.

The resulting F_z variance, including both the prior and posterior information, is then[24,46]

$$\mathrm{var}(F_z') = \frac{1}{\mathrm{var}^{-1}(F_z) + \mathrm{var}_{\mathrm{RO}}^{-1}(F_z)} = \frac{\mathrm{var}(F_z)}{1 + 2g^2|\langle S_x\rangle|\mathrm{var}(F_z)}$$

Expanding in g this becomes

$$\mathrm{var}(F_z') = \mathrm{var}(F_z) - 2g^2|\langle S_x\rangle|\mathrm{var}^2(F_z) + \mathcal{O}(g)^4 \tag{7}$$

Collecting equations (5)–(7), defining $\Delta\langle F_\alpha\rangle \equiv \langle F'_\alpha\rangle - \langle F_\alpha\rangle$ and $\Delta\mathrm{var}(F_\alpha) \equiv \mathrm{var}(F'_\alpha) - \mathrm{var}(F_\alpha)$, and dropping terms of order g^4 we find

$$\begin{aligned}\Delta\langle F_y\rangle &= -\frac{1}{2}g^2\big|\langle S_x\rangle\big|\langle F_y\rangle\\ \Delta\mathrm{var}(F_x) &= g^2\big|\langle S_x\rangle\big|\left[-\frac{1}{4}\mathrm{var}(F_x)+\frac{1}{2}\langle F_y^2\rangle\right]\\ \Delta\mathrm{var}(F_y) &= g^2\big|\langle S_x\rangle\big|\left[-\frac{1}{4}\mathrm{var}(F_y)+\frac{1}{2}\mathrm{var}(F_x)\right]\\ \Delta\mathrm{var}(F_z) &= -2g^2\big|\langle S_x\rangle\big|\mathrm{var}^2(F_z)\end{aligned}$$

Considering an initial coherent spin state and choosing $\big|\langle S_x\rangle\big| = g^{-2}N^{-1}$, where N is the number of spins, we note that $\Delta\mathrm{var}(F_z)\sim N$, which implies a reduction in the uncertainty of F_z relative to its initial uncertainty. Owing to the $\langle F_y^2\rangle$ term, the increase in $\mathrm{var}(F_x)$ is $\sim N$, comparable to its initial value. The other changes are ~ 1, which are negligible relative to the initial values. In this way we see that uncertainty is moved from F_z to F_x with negligible effect on F_y.

Larmor precession then noiselessly rotates uncertainty from F_y into F_z, uncertainty that is moved into F_x by the next measurement. This procedure reduces the uncertainty of both F_y and F_z with negligible influence from measurement back-action.

Implementation in an atomic ensemble. *Experimental set-up*. The experimental set-up is described in detail in refs 30,32. The trap consists of a single beam laser at 1,064 nm with 6.3 W of optical power, focused to a beam waist of 26 μm using an 80-mm lens. The trap is loaded with laser-cooled atoms from a magneto-optical trap (MOT). After sub-Doppler cooling in the final stage of the loading sequence, the trapped atoms have a temperature of about 12 μK. The resulting atomic ensemble has an approximately Lorentzian density distribution along the trap axis (which we label the z axis), with a full-width at half-maximum (FWHM) of 4 mm, and a Gaussian distribution in the transverse direction with a FWHM of 33 ± 3 μm.

State preparation. The initial atomic state is prepared via optical pumping with circularly polarized light resonant with the $F=1\rightarrow F'=1$ transition propagating along the y axis. During the optical pumping stage, the atoms are also illuminated with repumping light resonant with the $F=2\rightarrow F'=2$ transition using the six MOT beams, preventing accumulation of atoms in the $F=2$ hyperfine level, and a small magnetic field is applied along the x axis, with $B_x=37.6$ mG, to coherently rotate the atomic spins in the y–z plane. We use a stroboscopic pumping strategy, chopping the optical pumping light into a series of pulses of duration $\tau_{\mathrm{pump}}=1.5$ μs, applied synchronously with the precessing atoms for a total of 200 μs, to prepare the atoms in an F_y-polarized state with high efficiency (about 98%), resulting in an input polarized atomic ensemble with $\langle F_y\rangle \approx N$ (see Extended Data Fig. 1). The pulse duration $\tau_{\mathrm{pump}} \ll T_{\mathrm{L}}$ is chosen to optimize the optical pumping efficiency.

Probing. We probe the atoms via off-resonant paramagnetic Faraday rotation using pulses of linearly polarized light with durations of $\tau=0.6$ μs and a detuning of 700 MHz to the red of the ^{87}Rb D_2 line. The probe pulses are vertically (v)-polarized, with on average $N_{\mathrm{L}}=2.74\times10^6$ photons, and sent through the atomic cloud at 3-μs intervals. Between the probe pulses, we send horizontally (h)-polarized compensation pulses with on average $N_{\mathrm{L}}^{(\mathrm{h})}=1.49\times10^6$ photons through the atomic cloud. As described in detail in refs 12,13,24, the compensation pulses serve to cancel effects due to the tensor light shift, but do not otherwise contribute to the measurement. During the probing sequence, a magnetic field along the x direction drives a coherent rotation of the atoms in the y–z plane with a period of $T_{\mathrm{L}}=38$ μs. This ensures that the time taken to complete a single-pulse measurement is small compared to the Larmor precession period: $\tau \ll T_{\mathrm{L}}$.

We correct for slow drifts in the polarimeter signal by subtracting a baseline $\varphi_0=\frac{1}{N}\sum_{k=1}^{N}\varphi_k^{(i)}$ from each pulse, estimated by repeating the measurement without atoms in the trap.

Statistics of probing inhomogeneously coupled atoms. We consider the statistics of Faraday rotation measurements on an ensemble of N atoms, described by individual spin operators $\boldsymbol{f}_i$. To define the SQL, we consider an ensemble in a coherent spin state, in which the individual spins are independent and fully polarized in the F_y–F_z plane. We take N to be Poisson-distributed. When the spatial structure of the probe beam is taken into account, the Faraday rotation is described by the input–output relation for the Stokes component S_y:

$$S_y^{(\mathrm{out})} = S_y^{(\mathrm{in})} + S_x^{(\mathrm{in})}\sum_{i=1}^{N} g(\boldsymbol{x}_i)f_z^{(i)}$$

where $g(\boldsymbol{x}_i)$ is the coupling strength for the ith atom, proportional to the intensity at the location $\boldsymbol{x}_i$ of the atom. $S_y^{(\mathrm{in})}$ is has zero mean and variance $\big|\langle S_x^{(\mathrm{in})}\rangle\big|/2$. We first consider the case in which the spin is orthogonal to the measured F_z direction, that is, a measurement of the azimuthal component. Here the uncertainty in $g(\boldsymbol{x}_i)$ and in N make a negligible contribution, and the rotation angle $\varphi = S_y^{(\mathrm{out})}/S_x^{(\mathrm{in})}$ has the statistics

$$\begin{aligned}\langle\varphi\rangle &= \langle f_z\rangle\sum_{i=1}^{N}\langle g(\boldsymbol{x}_i)\rangle_{\boldsymbol{x}i}\\ &\equiv \langle N\rangle\langle f_z\rangle\mu_1\\ \mathrm{var}(\varphi) &= \mathrm{var}(\varphi_0)+\mathrm{var}(f_z)\left\langle\sum_{i=1}^{N}g^2(\boldsymbol{x}_i)\right\rangle_{N,\boldsymbol{x}_i}\\ &\equiv \mathrm{var}(\varphi_0)+\langle N\rangle\mathrm{var}(f_z)\mu_2\end{aligned}$$

where φ_0 is the polarization angle of the input light, subject to shot-noise fluctuations and assumed to be independent of F_z, and the angle brackets indicate an average over the number and positions of the atoms.

Next we consider the case in which the spin is along the measured F_z direction, that is, a measurement of the radial component. In this case, the uncertainty in f_z is zero, and the variation in g and in N determines the measured variation

$$\begin{aligned}\langle\varphi\rangle &= \langle N\rangle\langle f_z\rangle\mu_1\\ \mathrm{var}(\varphi) &= \mathrm{var}(\varphi_0)+\langle f_z\rangle^2\mathrm{var}\left[\sum_{i=1}^{N}g(\boldsymbol{x}_i)\right]\\ &\equiv \mathrm{var}(\varphi_0)+\langle N\rangle\langle f_z\rangle^2\nu_2\end{aligned}$$

We note that ν_2 includes the variation of both the atom number and the coupling strength, and as such is lower-bounded by the Poisson statistics of N: $\nu_2 \geq \langle g^2(\boldsymbol{x})\rangle = \mu_2$.

For known $\langle f_z\rangle$ and $\mathrm{var}(f_z)$, measurements of $\langle\varphi\rangle$ and $\mathrm{var}(\varphi)$ versus N give the calibration factors μ_1 and μ_2, as described in Methods subsections 'Measurement of calibration factor μ_1' and 'Measurement of calibration factor μ_2', respectively. To preserve the SQL $\mathrm{var}(F_z)=\big|\langle F_y\rangle\big|/2$ and similar, in the analysis leading to Fig. 2 we infer mean values as

$$\left\langle F^{(a)}\right\rangle = \frac{1}{\mu_1}\left\langle\varphi^{(a)}\right\rangle$$

and covariances, including $\mathrm{cov}(A,A)=\mathrm{var}(A)$, as

$$\mathrm{cov}\left(F^{(a)},F^{(b)}\right) = \frac{1}{\mu_2}\mathrm{cov}\left(\varphi^{(a)},\varphi^{(b)}\right)$$

where $F^{(a,b)}$ and $\varphi^{(a,b)}$ are corresponding spin and angle variables. Because the contribution of $\mathrm{var}(\varphi_0)$ is not subtracted, this overestimates the spin variances.

Measurement of calibration factor μ_1. We calibrate the measured rotation angle φ with dispersive atom number measurements using absorption imaging, as shown in Extended Data Fig. 2. For the absorption imaging, atoms are transferred into the $f=2$ hyperfine ground state by a 100-μs pulse of laser light tuned to the $5S_{1/2}(f=1)\rightarrow 5P_{3/2}(f'=2)$ transition. The dipole trap is switched off to avoid spatially dependent light shifts. An image is taken with a 100-μs pulse of circularly polarized light resonant to the $5S_{1/2}(f=2)\rightarrow 5P_{3/2}(f'=3)$ transition. We calculate the resonant interaction cross-section and take into account the finite observable optical depth. The statistical error in the absorption imaging is $<3\%$, including imaging noise and shot-to-shot trap loading variation.

Measurement of calibration factor μ_2. To measure μ_2 we prepare a F_y-polarized state by optical pumping, and then probe stroboscopically with $N_{\mathrm{p}}=36$ pulses of $N_{\mathrm{L}}=3.15\times10^7$ photons each in the presence of a B-field of approximately 71.5 mG along y, producing a Larmor precession of an angle π during the 10-μs pulse repetition period. In this way, the measured variable is always $\pm F_z$, evading back-action effects.

If φ_n is the measured Faraday rotation angle for pulse n, and $\varphi_0^{(n)}$ is the corresponding input angle, then we can define the pulse-train-averaged rotation signal as

$$\varphi \equiv \frac{1}{N_{\mathrm{p}}}\sum_{n=1}^{N_{\mathrm{p}}}(-1)^{n-1}\varphi_n$$

with variance

$$\mathrm{var}(\varphi) \equiv \mathrm{var}(\varphi_0)+\mu_2\sum_{n=1}^{N_{\mathrm{p}}}\mathrm{var}(F_{z,n})$$

where $\varphi_0 = \frac{1}{N_p}\sum_{n=1}^{N_p}\varphi_0^{(n)}$, with zero mean and variance $\mathrm{var}(\varphi_0) = (N_p N_L)^{-1}$, and $F_{z,n}$ is the value of F_z at the time of the nth probe pulse.

During the measurement, off-resonant scattering of probe photons both produces a reduction in the number of probed atoms and introduces noise into $\boldsymbol{F}$. We note that this is a single-atom process that preserves the independence of the atomic spins. We compute the resulting evolution of the state using the covariance matrix methods reported in ref. 24, and described specifically for this case in Methods subsection 'Calculation of the noise contribution α', giving

$$\mathrm{var}\left(\frac{g}{N_p}\sum_{n=1}^{N_p}F_{z,n}\right) = \mu_2\frac{1}{2}\alpha N$$

where $1/2 = \mathrm{var}(f_z)$ is the variance of the initial state and $\alpha = 0.86$ describes the net noise reduction due to scattering.

Including the readout noise $\mathrm{var}(\varphi_0)$ and a generic technical noise a_2N^2 in the preparation of the coherent spin state, we have the observable variance

$$\mathrm{var}(\varphi) = \mathrm{var}(\varphi_0) + \mu_2\frac{1}{2}\alpha N + a_2N^2 \quad (8)$$

in which the N scaling distinguishes the atomic quantum noise from other contributions. Experimental results shown in Extended Data Fig. 3 give $\mu_2 = (1.5 \pm 0.2)\times 10^{-14}$.

Calculation of the noise contribution α. As reported in ref. 24, the full system is described by a state vector $V = \left\{F_z, S_y^{(1)}, S_y^{(2)}, \ldots, S_y^{(N)}\right\}$ and covariance matrix $\Gamma = \langle V\wedge V + (V\wedge V)^{\mathrm{T}}\rangle/2 - \langle V\rangle\wedge\langle V\rangle$, where S_y^n is the measured photon imbalance after the nth pulse. The QND interaction leads to a transformation of the covariance matrix

$$\Gamma^{(n+1)} = M^{(n)}\Gamma^{(n)}\left[M^{(n)}\right]^{\mathrm{T}}$$

where M is equal to the identity matrix apart from the elements $M_{1,1} = -1$ due to the precession by an angle π about the magnetic field, and $M_{n+1,1} = gS_x$, where $S_x = N_L/2$, N_L is the number of photons per pulse and g is the coupling constant for uniform coupling.

Off-resonant scattering of photons introduces decoherence, noise and loss in the atomic state. During the spin-noise measurement, a fraction $\xi = 1 - \exp(-\eta N_L) = 0.01$ of atoms scatter a photon during a single probe pulse, where $\eta = 3\times 10^{-10}$ is the scattering rate per photon measured in an independent experiment, while a fraction $\chi = 1 - \xi$ remain in the coherent spin state. The scattered atoms are either lost from the $F = 1$ manifold, or return to $F = 1$ with probability $P = 0.7$ and random polarization. This has the effect of losing atomic polarization at each measurement. We calculate the effective measured polarization in terms of the initial atom number. We assume that the fraction p of scattered atoms that return to $F = 1$ have a random polarization and that the scattering rate η is independent of the atomic state.

After each pulse, the atomic part of the covariance matrix transforms according to

$$\Gamma_{\mathrm{at}}^{(n+1)} = \chi\Gamma_{\mathrm{at}}^{(n)} + \frac{2}{3}p(1-\chi)N^{(n)}\mathbb{I}$$

where $\mathbb{I}$ is the identity matrix. This follows from equation (A.6) of ref. 24, assuming $\Gamma_\Lambda = N\Gamma_\lambda$. We have

$$N^{(n+1)} = 1 - (1-\chi)(1-p)N^{(n)} = (\chi + p - \chi p)N^{(n)}$$

which, assuming that $N^{(0)} = N$, gives

$$N^{(n)} = (\chi + p - \chi p)^n N$$

Including these terms, we get a linear transformation of the covariance matrix after the nth pulse:

$$\Gamma^{(n+1)} = DM^{(n)}\Gamma^{(n)}\left[M^{(n)}\right]^{\mathrm{T}}D^T + N^{(n)}$$

where D is the identity matrix apart from the element $D_{1,1} = \sqrt{\chi}$, and $N^{(n)}$ is the zero matrix apart from the element $N_{1,1}^{(n)} = \frac{2}{3}p(1-\chi)(\chi + p - \chi p)^n N$.

We sum N individual polarimeter signals $S_y'^{(n)}$ to find the net Stokes operator $S_y' \equiv \sum_{n=1}^{N}(-1)^{n-1}S_y'^{(n)}$. This has a variance

$$\mathrm{var}(S_y') = \sum_{n=1}^{N}\mathrm{var}\left(S_y'^{(n)}\right) + 2\sum_{n\neq m}^{N}\mathrm{cov}\left(S_y'^{(n)}, S_y'^{(m)}\right)(-1)^{n-m} = P\Gamma^{(N)}P$$

with the projector $P = \mathrm{diag}(0, 1, -1, 1, -1, \ldots, -1)$. When evaluated analytically using $\chi = 0.99$, this gives

$$\mathrm{var}(S_y') = \mathrm{var}(S_{y,0}) + \beta g^2\frac{1}{2}NN_L^2 \quad (9)$$

where $\beta \approx 0.1081$. Noting that $\mathrm{var}(\varphi) = \mathrm{var}(S_y')/S_x^2$, where $S_x \equiv \sum_{n=1}^{N}S_x^{(n)}$ is the total input Stokes operator, dividing equation (9) by $S_x^2 = N_L^2/4$, and comparing against equation (8), we find that $\alpha = 8\beta \approx 0.86$.

Data analysis. *Fitting procedure.* As described in the main text, we follow a two-step fitting procedure in our data analysis: we first fit equation (2) to the joint dataset $\{\varphi(t_k)\}$ of the first and second measurements, to estimate the classical parameters g, ω_L, T_2 and φ_0 near the measurement time t_e; then, second, with the classical parameters fixed, we obtain a predictive estimate $\boldsymbol{F}_1$ using measurements $\{\varphi(t_k)\}_{t_e-\Delta t\le t_k<t_e}$ from the interval Δt immediately before t_e, and a confirming estimate $\boldsymbol{F}_2$ using $\{\varphi(t_k)\}_{t_e\le t_k<t_e+\Delta t}$ from the interval Δt after t_e.

Measurement phase. As shown in Fig. 2, the observed squeezing is independent of the choice of t_e, provided that sufficient measurements are available in the interval Δt before t_e, indicating that the observed squeezing is not dependent on the choice of a particular phase of the spin oscillation.

Fit gain. Because the classical parameters g, ω_L, T_2 and φ_0 are fixed beforehand, the predictive and confirming fits to estimate F_y and F_z are linear, least-squares fits to disjoint datasets. Our condition for (conditional) spin squeezing is whether the conditional variance $\mathrm{tr}(\Gamma_{\boldsymbol{F}_2|\boldsymbol{F}_1})$ is below classical limits—that is, whether the estimate $\boldsymbol{F}_1$ can be used to precisely predict the estimate $\boldsymbol{F}_2$. This definition of squeezing is quite robust with regard to the choice of estimators for F_y and F_z: they need only to have the right gain, that is, the slope of the curve relating the mean estimate to the true value. The error propagation formula can then be used to find the variance of the true values in terms of the variance of the estimators.

We check that the least-squares fits give the correct gain by comparing the estimated $\boldsymbol{F}_{1,2}$ with the results of two independent fits using all of the free parameters in equation (2). Results, shown in Extended Data Fig. 4, show that the gains are equal to within an approximately 10^{-3} fractional error, implying a similarly small, approximately 10^{-3} fractional error in the inferred variances and conditional variances, with negligible effect on the squeezing results.

Weights. For the first fit to estimate the classical parameters, our data are weighted using an empirical function based on two observations: (1) the polarimeter signal shows increased technical noise in the optical variable at larger imbalance, that is, when measuring a large instantaneous spin-projection along the z axis; and (2) points closer in time to t_e should be given greater weight (minimizing errors introduced by small changes in ω_L and T_2 during the measurement). This motivates using the weight function

$$W(\varphi(t_k)) \equiv \frac{g(|t_k - t_e|)}{h(\varphi(t_k))}$$

where $g(|t_k - t_e|) \equiv 1 + A\exp(-w|(t_k - t_e)/T_2|)$ and $h(\varphi_k) = 1 + r|\varphi_k|$. This ensures that we accurately estimate the classical parameters g, ω_L, T_2 and φ_0 at the measurement time t_e.

We numerically optimize $W(\varphi(t_k))$ by varying the parameters A, w and r and minimizing the resulting $\mathrm{tr}(\Gamma_{\boldsymbol{F}_2|\boldsymbol{F}_1})$ from the predictive and confirming fits. We find an optimum with the parameters $A = 15$, $w = 11$ and $r = 6$; the fit procedure gives similar results with variations of up to 30% in each of these parameters.

For the predictive and confirming fits, which are linear in F_y and F_z, all of the points are weighted equally.

Optimal measurement length. The optimal measurement length Δt results from a trade-off between the photon shot noise, the decoherences induced by the probing and the technical noise induced by the magnetic field. Longer measurements reduce the photon shot noise, while increasing the atomic decoherences and making the model in equation (2) less accurate. We empirically find the optimal Δt by minimizing the total variance $\mathrm{tr}(\Gamma_{\boldsymbol{F}_2|\boldsymbol{F}_1})$ for measurements with different length, as shown in Extended Data Fig. 5.

Conditional covariance. Estimating $\boldsymbol{F}$ for several values of t_e gives a predictive trajectory and a confirming one. Estimations are repeated on 453 repetitions of the experiment to gather statistics. Assuming Gaussian statistics, to quantify the measurement uncertainty we compute the conditional covariance matrix

$$\Gamma_{\boldsymbol{F}_2|\boldsymbol{F}_1} = \Gamma_{\boldsymbol{F}_2} - \Gamma_{\boldsymbol{F}_2\boldsymbol{F}_1}\Gamma_{\boldsymbol{F}_1}^{-1}\Gamma_{\boldsymbol{F}_1\boldsymbol{F}_2}$$

which quantifies the error in the best linear prediction of $\boldsymbol{F}_2$ based on $\boldsymbol{F}_1$ (ref. 47). Here $\Gamma_{\boldsymbol{v}}$ indicates the covariance matrix for vector $\boldsymbol{v}$ and $\Gamma_{\boldsymbol{uv}}$ indicates the cross-covariance matrix for vectors $\boldsymbol{u}$ and $\boldsymbol{v}$. The difference between the best linear prediction of $\boldsymbol{F}$ using $\boldsymbol{F}_1$ and the confirming estimate $\boldsymbol{F}_2$ is visualized using the vector $\boldsymbol{\mathcal{F}} = \{\mathcal{F}_y, \mathcal{F}_z\} = \tilde{\boldsymbol{F}}_2 - \Gamma_{\boldsymbol{F}_2\boldsymbol{F}_1}\Gamma_{\boldsymbol{F}_1}^{-1}\tilde{\boldsymbol{F}}_1$, where $\tilde{\boldsymbol{F}}_i = \boldsymbol{F}_i - \langle\boldsymbol{F}_i\rangle$. Standard errors in

the estimated conditional covariance matrix are calculated from the statistics of $\{\mathcal{F}\}$ (ref. 48).

Data availability. The datasets generated and analysed during this study are available from the corresponding author on reasonable request. The data shown in Fig. 2 and all of the data used to generate the plots in Extended Data Figs 1–5 are provided as Source Data.

32. Kubasik, M. *et al.* Polarization-based light-atom quantum interface with an all-optical trap. *Phys. Rev. A* **79,** 043815 (2009).
33. Deutsch, I. H. & Jessen, P. S. Quantum control and measurement of atomic spins in polarization spectroscopy. *Opt. Commun*. **283,** 681–694 (2010).
34. Kuzmich, A., Mandel, L. & Bigelow, N. P. Generation of spin squeezing via continuous quantum nondemolition measurement. *Phys. Rev. Lett*. **85,** 1594–1597 (2000).
35. Appel, J. *et al.* Mesoscopic atomic entanglement for precision measurements beyond the standard quantum limit. *Proc. Natl Acad. Sci. USA* **106,** 10960–10965 (2009).
36. Gühne, O. & Tóth, G. Entanglement detection. *Phys. Rep*. **474,** 1–6 (2009).
37. Sørensen, A. S. & Mølmer, K. Entanglement and extreme spin squeezing. *Phys. Rev. Lett.* **86,** 4431–4434 (2001).
38. Schlosser, N., Reymond, G., Protsenko, I. & Grangier, P. Sub-poissonian loading of single atoms in a microscopic dipole trap. *Nature* **411,** 1024–1027 (2001).
39. Hofmann, C. S. *et al.* Sub-Poissonian statistics of Rydberg-interacting dark-state polaritons. *Phys. Rev. Lett.* **110,** 203601 (2013).
40. Gajdacz, M. *et al.* Preparation of ultracold atom clouds at the shot noise level. *Phys. Rev. Lett.* **117,** 073604 (2016).
41. Stockton, J. K. *Continuous Quantum Measurement of Cold Alkali-atom Spins*. PhD thesis, California Institute of Technology (2007).
42. Takano, T., Fuyama, M., Namiki, R. & Takahashi, Y. Spin squeezing of a cold atomic ensemble with the nuclear spin of one-half. *Phys. Rev. Lett.* **102,** 033601 (2009).
43. Schleier-Smith, M. H., Leroux, I. D. & Vuletić, V. States of an ensemble of two-level atoms with reduced quantum uncertainty. *Phys. Rev. Lett.* **104,** 073604 (2010).
44. Sewell, R. J. *et al.* Magnetic sensitivity beyond the projection noise limit by spin squeezing. *Phys. Rev. Lett.* **109,** 253605 (2012).
45. Bohnet, J. G. *et al.* Reduced spin measurement back-action for a phase sensitivity ten times beyond the standard quantum limit. *Nat. Photon*. **8,** 731–736 (2014).
46. Madsen, L. B. & Mølmer, K. Spin squeezing and precision probing with light and samples of atoms in the Gaussian description. *Phys. Rev. A* **70,** 052324 (2004).
47. Behbood, N. *et al.* Generation of macroscopic singlet states in a cold atomic ensemble. *Phys. Rev. Lett.* **113,** 093601 (2014).
48. Kendall, M. & Stuart, A. *The Advanced Theory of Statistics* Vol. 1, Ch. 9 (Griffin, 1979).

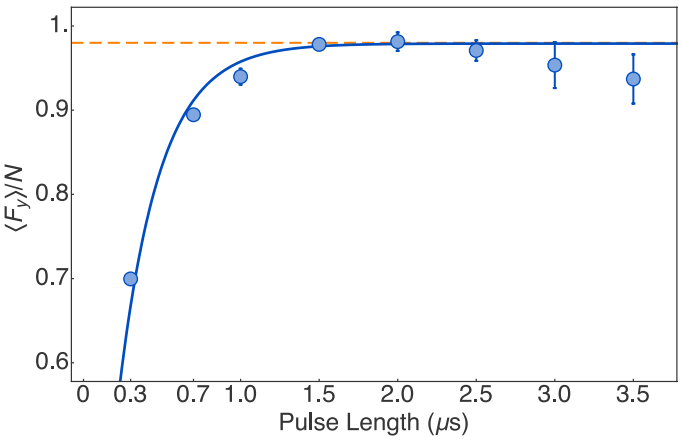

Extended Data Figure 1 | Optical pumping efficiency. We prepare an input atomic state with $\langle F_y \rangle \approx N$ via stroboscopic optical pumping in the presence of a small magnetic field along the x axis. Data are fitted with the exponentially growing curve $a(1 - e^{-t/\tau})$ (solid line); we obtain $a = 0.979 \pm 0.004$ and $\tau = 0.26 \pm 0.02$. The orange dashed line shows the optical pumping efficiency of 98%. Error bars (± 1 s.e.m.) are smaller than the points for most of the data.

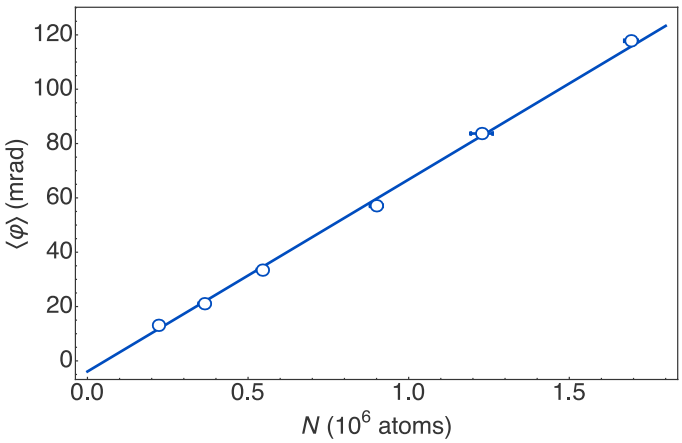

Extended Data Figure 2 | Calibration of average Faraday rotation signal. We calibrate the rotation angle φ against input atom number N, measured via absorption imaging. Solid line, the fit curve $\varphi = a_0 + \mu_1 N$, with which we obtain $\mu_1 = (7.07 \pm 0.04) \times 10^{-8}$ and $a_0 = (3.9 \pm 0.3) \times 10^{-3}$. Error bars, ± 1 s.e.m.

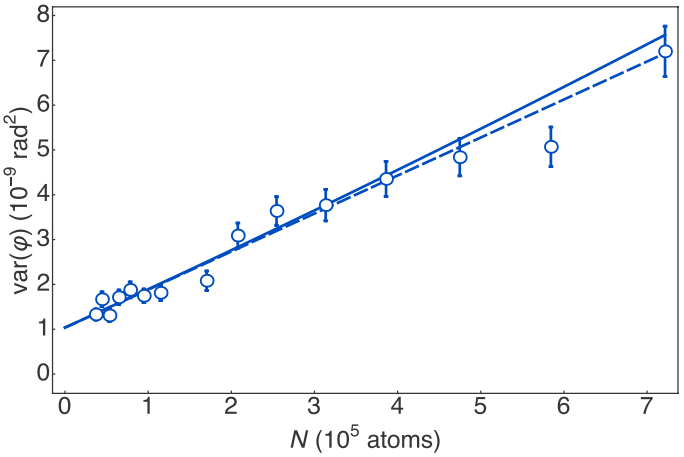

Extended Data Figure 3 | Calibration of quantum-noise-limited Faraday rotation probing of atomic spins. We plot the measured variance $\mathrm{var}(\varphi)$ as a function of the number of atoms N in an input coherent spin state with $\langle \boldsymbol{F} \rangle = \{0, N, 0\}$. Solid curve, a fit using the polynomial $\mathrm{var}(\varphi) = a_0 + a_1 N + a_2 N^2$. The linear term $a_1 = \alpha \mu_2 N/2$ corresponds to the atomic quantum noise from atoms in the input coherent spin state. We estimate $a_0 = (11.7 \pm 0.7) \times 10^{-10}$, $a_1 = (6.5 \pm 0.8) \times 10^{-15}$ and $a_2 = (2.8 \pm 12) \times 10^{-22}$, consistent with negligible technical noise in the atomic state preparation. Dashed line, $\mathrm{var}(\varphi) = a_0 + a_1 N$. Error bars indicate ± 1 standard error in the variance for 206 repetitions.

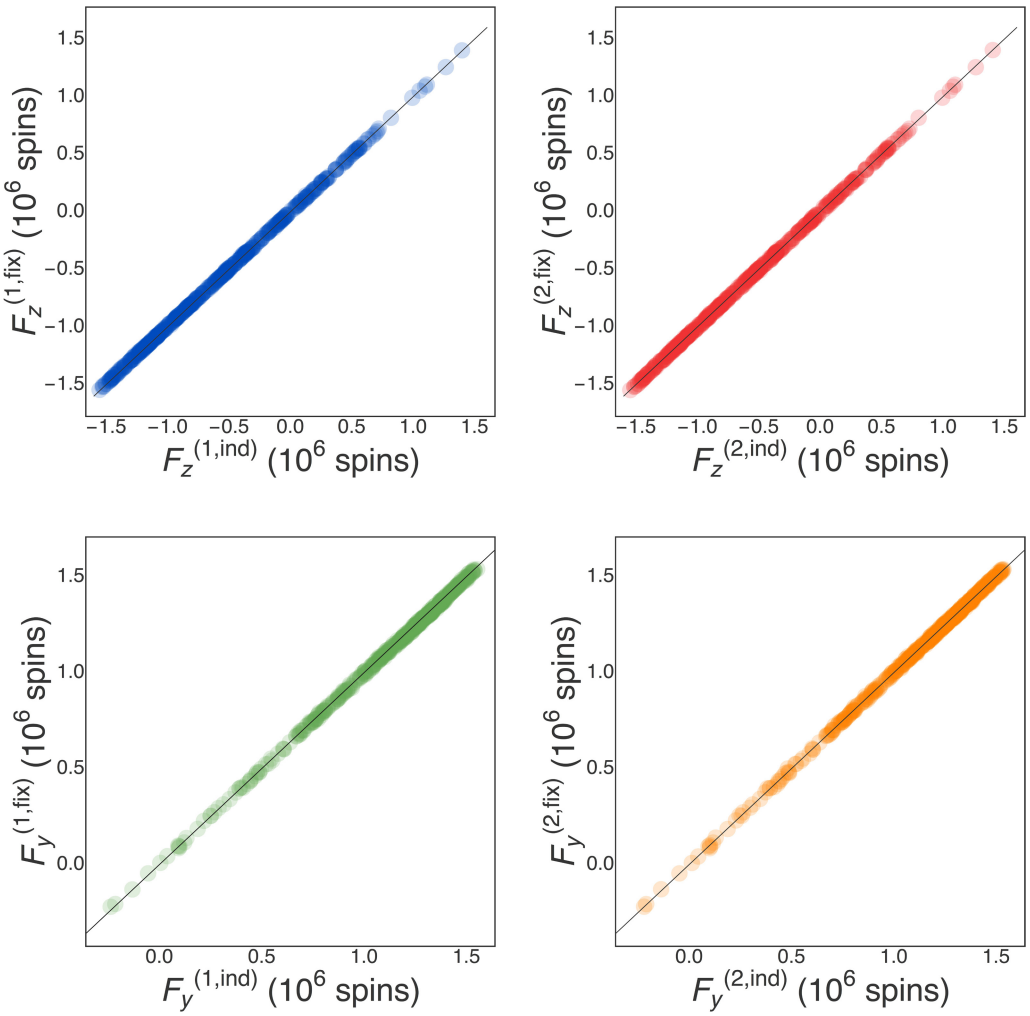

Extended Data Figure 4 | Fit gain. We compare the estimated F_z and F_y from a fit using equation (2): first, with the classical parameters g, ω_L, T_2 and φ_0 fixed (labelled $F_{y,z}^{(n,\mathrm{fix})}$) for measurements $n=1$ and 2; and second, with these parameters free to vary as independent parameters (labelled $F_{y,z}^{(n,\mathrm{ind})}$). Blue (green), F_z (F_y) of the first measurement; red (orange), F_z (F_y) of the second measurement. A linear fit $\gamma x+\delta$ to points in plots a–d gives $\gamma_a=0.9981(8)$, $\gamma_b=1.0026(8)$, $\gamma_c=0.9923(4)$ and $\gamma_d=1.0007(5)$, and $\delta_a=0.003(1)$, $\delta_b=0.0001(9)$, $\delta_c=0.0004(3)$ and $\delta_d=-0.0023(3)$. A grey line $y=x$ is plotted for comparison in each panel.

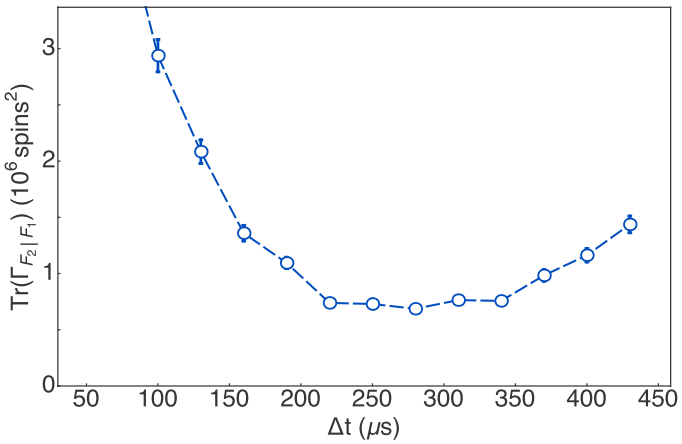

Extended Data Figure 5 | Tracking precision as function of Δt. An optimum is found at $\Delta t = 270\,\mu s$. Error bars indicate ± 1 standard error in the variance for 453 repetitions.